Enhanced Phosphate Removal from Water Using Iron-Nanoparticle Impregnated Ion Exchange Resin (FerrIX A33E): Batch and Column Studies

Sedar Dogan[1], Graham Smith[2], Chedly Tizaoui[*1]

[1]Water and Resources Recovery Research Lab, Faculty of Science and Engineering, Department of Chemical Engineering, Swansea University, Bay Campus, Fabian Way, Swansea, SA1 8EN, UK

[2]Tata Steel, Port Talbot, SA13 2NG, UK

[*]Correspondence to: c.tizaoui@swansea.ac.uk; ORCID: 0000-0003-2159-7881

Statements and Declarations

Funding: The authors acknowledge the Materials and Manufacturing Academy (M2A) funding from the European Social Fund via the Welsh Government (c80816), Swansea University, and Tata Steel.

Author contributions: All authors contributed to the study conception and design and all authors read and approved the final manuscript.

Sedar Dogan: Conceptualization; Data curation; Formal analysis; Investigation; Methodology; Visualization; Writing – original draft; **Graham Smith:** Conceptualization; Methodology; Project administration; Resources; Writing – review & editing; **Chedly Tizaoui:** Conceptualization; Formal analysis; Funding acquisition; Methodology; Project administration; Resources; Supervision; Visualization; Writing – review & editing

Competing interests: The authors have no relevant financial interests to disclose. Tizaoui is an Associate Editor of EMJEI.

Availability of data and material: All data generated or analysed during this study are available upon request.

Ethics approvals: Not applicable.

Enhanced Phosphate Removal from Water Using Iron-Nanoparticle Impregnated Ion Exchange Resin (FerrIX A33E): Batch and Column Studies

Abstract

The release of phosphate into water bodies promotes eutrophication and disrupts water treatment processes, highlighting the need for efficient phosphate removal technologies in water systems. This study examines the performance of FerrIX A33E, an iron nanoparticle-impregnated strong-base anion exchange resin, for phosphate removal in water using batch and fixed-bed column ion exchange experiments. The Freundlich equation fitted the isotherm data well (R^2>0.999), with the coefficients K_f = 3.621 (mg P)$^{0.7805}$L$^{0.2195}$g^{-1} and $1/n$ = 0.2195. Batch kinetic data were analysed using first-order reversible, Elovich, and particle diffusion models at varying mixing speeds, with the first-order reversible and Elovich models providing the best description of the experimental results. A dual mechanism for phosphate removal with FerrIX A33E involving ion exchange and sorption/complexation with iron oxides was suggested. To understand the effects of key operational parameters on column breakthrough curves (bed height, inlet concentration, and flowrate), conventional models including Bohart-Adams, Thomas and Clark models in conjunction with newly developed models B-A *n* order and fractal models were used to describe the experimental data. The B-A *n* order and fractal models were found most suitable due to the asymmetric nature of the breakthrough curves. The resin was successfully regenerated using 5% sodium chloride solution and repeated ion exchange/regeneration cycles did not significantly affect the average resin capacity. This study provides data useful for process design and demonstrates that nanoparticle iron impregnated ion exchange resin could offer a sustainable method to address the phosphate challenge in the aquatic environment.

Key words: Phosphates, phosphorus, ion exchange, Freundlich, fractal model, FerrIX A33E

1 Introduction

Elevated phosphate concentrations in surface waters promote excessive growth of algae and aquatic plants, thereby disrupting the ecological balance of aquatic environments (Bol et al., 2018, Wang et al., 2024). Excessive plant and algal growth can deplete dissolved oxygen in water bodies, adversely affecting aquatic life and degrading the overall ecological status of the ecosystem (Environment Agency, 2025). In England, for example, phosphorus is the number one reason for water bodies not achieving good ecological status (Environment Agency, 2019). With the ever more stringent legislations being introduced globally, such as the European Water Framework Directory (WFD), to control phosphates discharge into the aquatic environment, the removal of phosphates is an essential area of water research. The major sources of phosphate in surface water are agricultural activities, urbanization, and discharges from wastewater treatment plants (Carpenter et al., 1998, Bol et al., 2018, Environment Agency, 2025). Phosphate compounds can also originate from industrial processes, such as in the energy sector where they are added to boilers to control or inhibit scaling. However, their presence can interfere with ion exchange operations by reducing the selectivity of columns for target anions, such as reactive silica in boiler water. These phosphates can accumulate in boiler sludge blowdowns (Shokri and Sanavi Fard, 2023) and ultimately enter the environment through wastewater discharge. Consequently, phosphate removal from water is important not only for controlling eutrophication but also for improving efficiency and selectivity in certain industrial processes.

Various physical, chemical, and biological methods have been explored for phosphate removal from water, including membrane filtration, chemical precipitation, adsorption, and ion exchange (Ownby et al., 2021, Manawi et al., 2022, Thistleton et al., 2002, Zhang et al., 2023, Flores et al., 2026, Wang et al., 2024). Chemical dosing methods for phosphorus removal can

be costly, as achieving the stringent discharge standards, typically below 1 mg P/L, requires substantial quantities of treatment chemicals. On the other hand, adsorption-based technologies have been widely investigated for phosphate removal from water due to their simplicity, effectiveness, and potential for regeneration (Usman et al., 2022, Awual, 2019). Driven by the dual objectives of mitigating eutrophication and enabling the reuse of recovered phosphorus as a valuable resource, a wide range of adsorbents have been developed to remove and recover phosphates from wastewater. For instance, biochar, particularly when modified with metals such as Fe, Al, or Mg, offers a low-cost and sustainable option, achieving phosphate uptake capacities in the range of 5-30 mg P/g while enabling resource recovery (Ma et al., 2025, Luo et al., 2023, Lu et al., 2023, Yao et al., 2011). Layered double hydroxides (LDHs) exhibit high phosphate affinity through anion exchange and surface complexation, with reported capacities often reaching 50 mg P/g depending on metal composition and synthesis method (Goh et al., 2008, Das et al., 2006, Flores et al., 2026, Li et al., 2016). Metal oxides and hydroxides, such as iron, aluminium, and zirconium oxides, are among the most effective phosphate adsorbents due to their ability to form strong inner-sphere complexes with phosphate. However, their adsorption performance is often highly pH-dependent, and practical challenges remain in immobilising these fine particles into mechanically stable forms suitable for fixed-bed or column ion-exchange applications (Zhang et al., 2009, Wang et al., 2024, Liu et al., 2018). Despite their promise, variability in reported capacities and limited understanding of adsorption mechanisms under realistic water matrices highlight the need for systematic evaluation and improved modelling of these materials.

Ion exchange is a well-established technology in water treatment, and with recent developments, its efficiency for phosphate removal has been improved using newly developed ion exchangers such as ferric oxide nanoparticles infused resin. The advantages of ion exchange are its robustness and simple operation, while it could be easily integrated within a

wastewater treatment as a tertiary treatment or a polisher to remove phosphates. It is also advantageous since it produces no-excess sludge and as being reversible, the removed phosphorus could be directly recovered and processed into useful products, such as struvite for slow-release fertilisers (Yan et al., 2025). Moreover, the impregnation of the resin with ferric oxide nanoparticles to produce a hybrid anion exchanger increases its selectivity towards phosphate ions and its overall exchange capacity (Nur et al., 2014a, Yoon et al., 2014, Cross et al., 2009). Several studies have demonstrated that hybrid anion exchangers exhibit high selectivity for phosphate even in the presence of commonly encountered anions such as sulphate, chloride, and bicarbonate (Blaney et al., 2007, Martin et al., 2013, Sendrowski and Boyer, 2013). Importantly, phosphate uptake has been shown to be largely insensitive to sulphate concentration, which is typically the dominant competing anion in conventional ion-exchange processes. Reported phosphate-sulphate separation factors exceeding two orders of magnitude indicate a strong preferential affinity for phosphate over sulphate on these materials (Blaney et al., 2007).

FerrIX A33E (Purolite) is a strong-base anion exchange resin composed of a highly porous polystyrene matrix cross-linked with divinylbenzene and functionalised with positively charged quaternary ammonium groups. Originally developed for arsenic removal (PUROLITE, 2021), the resin incorporates iron oxide nanoparticles that impart high affinity for oxyanions; however, its application for phosphate removal has received relatively limited investigation. Moreover, the few studies that have investigated FerrIX A33E for phosphate removal report notable discrepancies in its capacity (Section 3.2 of this study) and regeneration performance, while the influence of operating conditions on resin uptake properties and column performance has not been thoroughly examined (Nur et al., 2014a, Foster et al., 2025, Bektaş et al., 2021, Korkmaz et al., 2023). Batch experiments by Nur et al. (2014a) reported maximum phosphate uptake capacity of approximately 48 mg P/g resin, while fixed-bed column modelling in Nur

et al. (2014b) indicated lower dynamic capacities that depended on bed height for a given inlet concentration. More recent work by Foster et al. (2025) showed that when regeneration efficiency and multi-cycle operation are considered, the effective capacity decreased from ~1.9 to ~1 mg P/mL (~2.6 to 1.4 mg P/g). These numerical discrepancies highlight the need to more rigorously establish the intrinsic phosphate removal capacity of FerrIX A33E under well-defined conditions. Furthermore, existing modelling efforts for fixed-bed phosphate removal appear limited, as the commonly applied models did not adequately capture the observed breakthrough behaviour, potentially leading to inaccurate predictions for scale-up. In particular, studies by (Nur et al., 2014a, Nur et al., 2014b) show clearly asymmetric breakthrough curves, which challenges the validity of conventional models that assume symmetrical breakthrough behaviour. This suggests that alternative modelling approaches capable of accounting for breakthrough asymmetry should be evaluated. In addition, systematic kinetic studies on phosphate uptake by FerrIX A33E are absent, and equilibrium data have been interpreted solely using the Langmuir isotherm without comparison to other models, such as the Freundlich isotherm, which better accounts for surface heterogeneity expected in hybrid iron oxide-impregnated resins. Given the growing interest in phosphate removal and recovery, there is a clear need for more robust kinetic, equilibrium, and dynamic models to accurately describe sorption processes and support reliable process design and scale-up of FerrIX A33E resin.

Therefore, this study evaluated the removal of phosphate by FerrIX A33E focusing on sorption capacity and kinetics, and breakthrough experiments in batch and fixed-bed modes, respectively. Common and newly adapted mathematical models were used to predict the isotherms, exchange kinetics, and column breakthrough curves. The results reported in this study enhance understanding of the performance of FerrIX A33E for phosphate removal and provide useful information for design and scaling up of the process.

153

154 2 Materials and methods

155 *2.1 Chemicals*

156 Analytical grade sodium phosphate monobasic monohydrate ($NaH_2PO_4.H_2O$) powder (Acros
157 Organics, UK) and sodium chloride (Sigma Aldrich, UK) were used to prepare aqueous
158 solutions in Milli Pore filtered water (MilliQ RiOs-DI 3UV). Phosphate stock solutions at
159 varying concentrations (6.5-66.67 mg P/L) representing low and high phosphate concentrations
160 were prepared. The ion exchange resin was FerrIX A33E (Purolite, USA), which is a type II
161 hybrid strong base anion exchange resin containing a blend of hydrated iron oxide
162 nanoparticles and highly porous polystyrene cross-linked with divinylbenzene polymer. The
163 resin has quaternary ammonium positively charged functional groups with chloride being the
164 counter ions. Other characteristics of the ion exchange resin used in this study are shown in
165 Table 1 according to the manufacturer's information sheet (PUROLITE, 2021) or determined
166 in this study.

167 *2.2 Ion exchange resin characterisation*

168 The total capacity of FerrIX A33E resin was determined using the pH titration technique.
169 Briefly, several samples, each containing 0.5 g of resin, which was initially treated with 1M
170 NaOH to convert it into the OH^- form, were placed in 50 mL flasks and mixed with successively
171 increasing volumes of HCl solution (0.1 M). Deionized water was added to keep the ratio of
172 solid to liquid constant (1:100 w/v). The pH was measured after equilibration over 24 hours.
173 Neutralization of the obtained acid or base solution was made, and the titration curve was
174 plotted as pH of the solution vs the amount of titrant added (meq HCl/g of resin). The total
175 capacity was determined at the point where the titration curve sharply increased.

Particle size measurements were conducted by passing the resin through sieves with pores in the range of 0.42 to 4 mm. Images of the resin particles were also taken using a Zeiss Primotech light microscope to confirm their sizes and shapes. The nitrogen adsorption/desorption at 77K was used to determine the surface area and the pore properties of the resin (Nova 2000e, Quantachrome Instruments, Boyton Beach, FL, USA). The Brunauer-Emmett-Teller (BET) model was used to determine the surface area, while the Barrett-Joyner-Halenda (BJH) model was used for pore size properties. Samples were degassed at 110°C with a vacuum pump for 3 hours to remove impurities such as water and were weighed before and after the degassing process.

Table 1. Characteristics of ion exchange resin FerrIX A33E (Purolite, USA)

Polymer matrix	Polystyrene crosslinked with divinylbenzene
Ionic Form	Cl^-
Appearance	Brown spherical beads
Particle size range	300-1200 µm
Bulk Density	0.74 g/cm^3
pH limits	4.5-8.5
Temperature limit	80 °C

2.3 Isotherm and kinetics studies

The isotherm experiments were carried out at room temperature (20±2^{o}C) using aqueous samples (40 mL) placed in 50mL-plastic sample tubes and agitated for 24 h using a 12-position rotating mixer (Stuart SB3 rotator) set at 40 rpm. The initial phosphate concentration was 20 mg P/L and the resin dose varied in the range 0.25 to 6.25 g/L. Phosphate uptake onto the resin was calculated by Equation (1), which was derived from mass balances over the liquid and resin phases assuming that any change in phosphate mass in the liquid phase was due to the resin uptake only.

$$q_e = V \times \frac{(C_o - C_e)}{m_{IX}} \quad (1)$$

where: q_e is the phosphate uptake onto the resin (mg P/g), V is the volume of solution (L), C_0 and C_e are the initial and equilibrium concentrations (mg P/L) respectively, and m_{IX} is the mass of the ion exchange resin (g).

Figure 1(a) shows the schematic layout of the set-up used for the kinetic experiments. The kinetic experiments were carried out using 500 mL solutions at a resin dose of 3.75 g/L and initial phosphate concentration of 16.67 mg P/L. The solutions were mixed using a six-paddle mixer (W1 flocculation test unit) set at different impeller speeds (50-150 rpm). Samples (~1mL) were collected and analysed for phosphate concentration using a microwave plasma atomic emission spectrometer (Agilent 4200 MP-AES). Samples were collected at regular time intervals and solution volume change due to sampling was considered in the calculation.

2.4 Column breakthrough

Dynamic semi-batch column ion exchange experiments were carried out using an ion exchange experimental rig (CE300, G.U.N.T, Germany); its layout is shown in Figure 1(b). The column internal diameter was 21.2 mm and the maximum column height was 40 cm. After thorough washing, the resin was added to the column under saturated water conditions to avoid air being trapped in the bed. The column was run in a down-flow mode and samples at the column exit were collected at regular intervals of time, analysed for phosphorous concentrations, and the results were used to plot the breakthrough curves (i.e. $x_b = C_t/C_0$ versus time). The range of variables used in the experiments were: flowrates (30-120 mL/min), bed height (5-10 cm), and influent concentrations (16-67 mg P/L).

2.5 Regeneration

The regeneration of the phosphate-saturated ion exchange was studied by flowing a 5% sodium chloride solution in the semi-batch column at a regenerant flow rate of 30 mL/min. The exchange/regeneration cycles were repeated 3 times for the same resin to evaluate the effect of resin reuse on phosphate exchange capacity. The data collected were presented as breakthrough curves of chloride ions during regeneration. The breakthrough curves were integrated to determine the amounts of chloride exchanged by the resin. The concentration of chloride was analysed using an ion chromatograph (Thermo Scientific Dionex Integrion HPIC) fitted with a Dionex IonPac AS29-Fast-4µm analytical column and a Dionex IonPac AG13A-5µm guard column. The eluent used was Dionex AS14A (8.0 mM sodium carbonate, 1.0mM sodium bicarbonate) with a set flowrate of 0.5 mL/min. The chloride solutions were diluted before analysis, so to not saturate the detector.

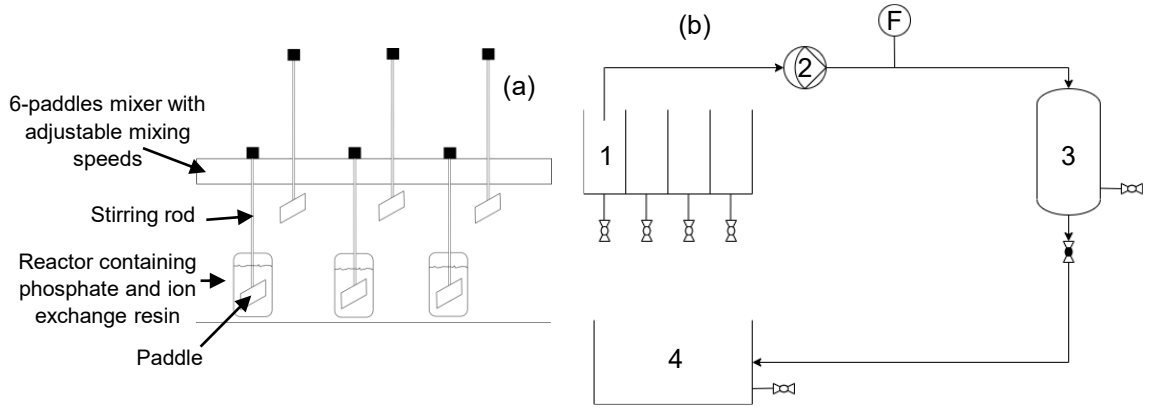

Figure 1: Schematic diagrams of (a) kinetics experiments, (b) fixed-bed column studies: 1 - collecting tank, 2 – diaphragm pump, 3 – Anion exchange column, 4 – waste tank, F – flowmeter.

3 Results and discussion

3.1 Resin characterisation

3.1.1 Particle size

The particle size distribution of the dry FerrIX A33E resin was determined by passing a representative sample through a series of standard sieves. Figure 2(a) shows the percent of the sample retained by the specified sieves. The data indicates a particle size range of approximately 0.3 to 1.8 mm, which aligns well with the specifications provided by the manufacturer (Table 1). The uniformity coefficient of the resin, d_{60}/d_{10}, was found equal to 1.36, indicating that the resin particles have uniform sizes and uniform shape as observed by the microscopic images (Figure 2(b)).

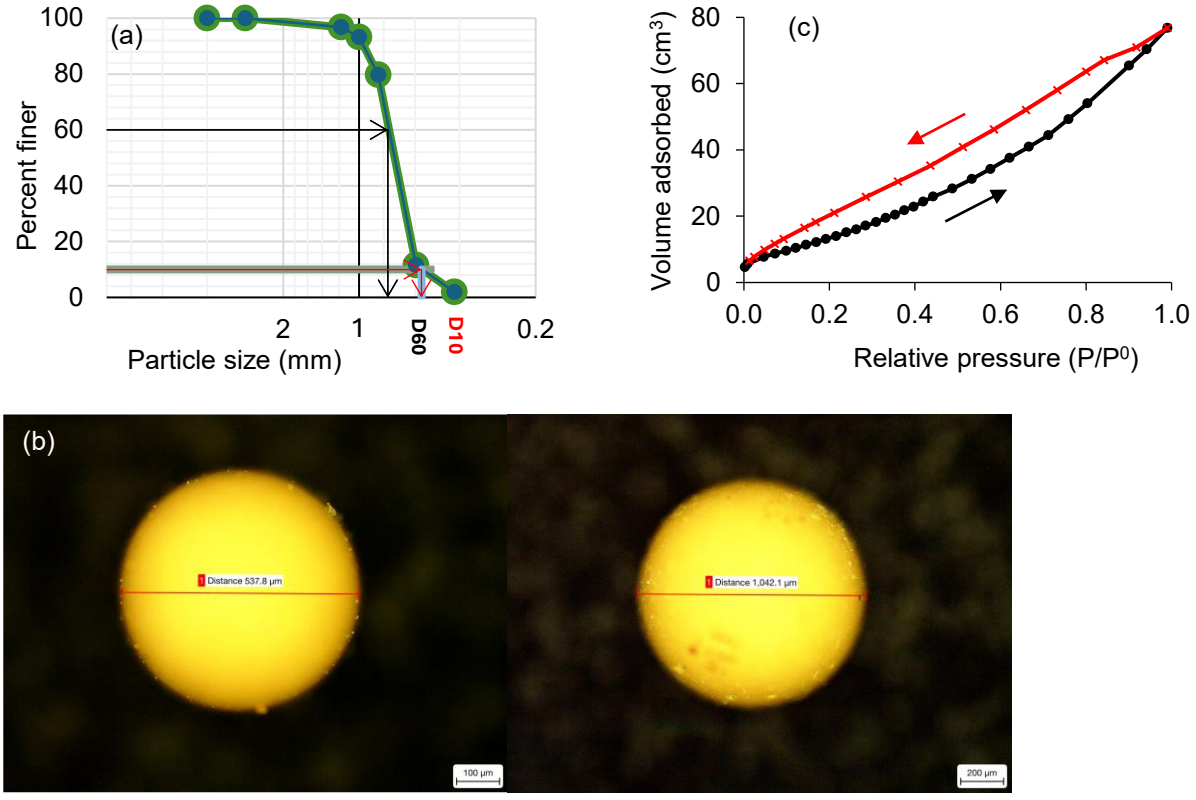

Figure 2. (a) FerrIX A33E resin particle size distribution; (b) microscopic image of the ion exchange particles: example of two sizes; (c) cryogenic nitrogen adsorption/desorption isotherms on FerrIX A33E resin

3.1.2 Surface area and pore volume

The BET results show that FerrIX resin has a surface area of 66.4 m^2/g, which is comparable to that reported by Thompson et al. (2021) for FerrIX (63.0 m^2/g), but considerably larger than other gel resins such as MERCK 104767 (25.0 m^2/g) (Mestri et al., 2023). The cryogenic nitrogen adsorption-desorption isotherm exhibited a Type H3 hysteresis loop (Figure 2(c)), indicative of a weak adsorbate-adsorbent interactions and associated with multimolecular adsorption (Thommes et al., 2015). The hysteresis observed in Figure 2(c) suggests desorption from large pores governed by cavitation-controlled evaporation, a behaviour characteristic of non-rigid aggregates of plate-like particles and the presence of meso- to microporous structures, as commonly found in mesoporous zeolites and clays. In addition, analysis using the BJH method yielded a pore volume of 0.119 cm^3/g and an average pore diameter of 3.28 nm, confirming that FerrIX possesses a predominantly mesoporous structure.

3.1.3 Total capacity and suitability for phosphates removal

The total exchange capacity of the FerrIX A33E resin was experimentally determined using the pH titration method. Because ion exchange resins are essentially insoluble in acidic and alkaline solutions, they can reach equilibrium during acid-base titration, allowing the total capacity to be quantified from the titration response. Initially, the solution of FerrIX A33E exhibited a high pH (~12) due to the resin being in the hydroxide form. Upon addition of hydrochloric acid, the hydroxide ions on the surface of the resin were gradually replaced by the chloride ions, resulting in a slow decrease in pH, as described by Eq (2). Once all the exchangeable hydroxide ions were fully displaced, further addition of acid caused a sharp drop in pH due to the presence of excess free acid. This rapid pH decrease, from approximately 11 to 3, occurred around a clear inflection point corresponding to the equivalence point, where the moles of added acid equated the total ion exchange capacity of the resin. Based on this analysis,

the total exchange capacity of FerrIX A33E was determined to be 1.2 meq HCl/g resin (or 0.9 eq/L), which compares to other macroporous polystyrene anionic resins such as Purolites A500 (1.15 eq/L) and A510 (1.2 eq/L).

$$\overline{R-OH} + HCl \rightarrow \overline{R-Cl} + H_2O \quad (2)$$

Although FerrIX™ A33E was originally developed for arsenic removal, it is also suitable for phosphate removal because both arsenate and phosphate share very similar chemical characteristics and binding mechanisms. On one hand, phosphate (PO_4^{3-}) and arsenate (AsO_4^{3-}) are structurally analogous tetrahedral oxyanions with comparable charge, size, and pKa values (phosphates: $pKa_1 = 2.12$, $pKa_2 = 7.21$, $pKa_3 = 12.44$; Arsenate: $pKa_1 = 2.22$, $pKa_2 = 6.98$, $pKa_3 = 11.53$), leading to similar sorption behaviour in water. On the other hand, FerrIX A33E is a hybrid strong-base anion quaternary ammonium exchange resin impregnated with hydrous iron oxide (HIO) nanoparticles, which provide highly specific surface sites for complexation with oxyanions. Although the quaternary ammonium groups facilitate conventional anion exchange, phosphate removal is dominated by strong ligand exchange reactions between phosphate ions and surface hydroxyl groups on the embedded iron oxide (Acelas et al., 2015, Almasri et al., 2019). This mechanism is identical to that responsible for arsenate binding (Dudek and Kołodyńska, 2022, Gonzalez-Pech et al., 2022) and explains the resin's high affinity for phosphate. Therefore, we refer to the mechanism as "sorption" to reflect that phosphate uptake by FerrIX A33E is neither purely ion exchange nor purely adsorption. In addition, the polymeric matrix enhances mass transfer and mechanical stability compared to granular iron oxides alone, making FerrIX A33E effective in fixed-bed columns. Consequently, the physicochemical similarities between arsenate and phosphate, combined with the dual ion-exchange and iron-oxide adsorption functionality of FerrIX A33E, make it well suited for phosphate removal despite its original design focus on arsenic.

3.2 Batch isotherm results

Sorption equilibrium isotherms were determined to quantify the uptake capacity of FerrIX A300E resin for phosphates. The experimental data were fitted using several isotherm models, including Langmuir, Freundlich, Dubinin-Radushkevich, and Redlich-Peterson. Application of these models provides insight not only into the exchange capacity but also into the underlaying resin properties and ion exchange mechanisms governing phosphate uptake. A summary of the equations and parameters of the models used is presented in Table 2 and the results of model fitting of the experimental data are shown on Figure 3. The uptake results show that the capacity of FerrIX A33E is around 6.5 mg P/g resin, which is comparable to other similar resins such as the HAIX (~6 mg P/g resin) (Guida et al., 2021).

According to Figure 3 and Table 2, only the Freundlich and Redlich-Peterson models exhibited good fitting of the experimental data. The Freundlich model assumes that adsorption takes place on a heterogenous surface and can be of multilayer while the Redlich-Peterson isotherm is a compromise of the Langmuir and Freundlich isotherms.

Several studies have investigated phosphate removal using ion exchange resins, and the corresponding equilibrium isotherm parameters reported in the literature are summarised in Table 3. Overall, the Freundlich isotherm provides the best fit for most of the resins examined, suggesting that phosphate uptake occurs on energetically heterogeneous surfaces rather than through ideal monolayer adsorption. This behaviour is consistent with the complex pore structures and varied functional groups present in commercial ion exchange resins.

As illustrated in Figure S1, substantial differences in phosphate uptake capacity are observed among the resins studied. Lewatit Monoplus M 600 and Purolite A200E exhibit notably higher capacities compared to the other materials, whereas AMBERLITE HPR9200 shows the lowest

phosphate uptake, with FerrIX A33E displaying intermediate performance. Despite all materials being classified as strong-base anion exchange resins, these pronounced discrepancies highlight that phosphate removal efficiency cannot be attributed solely to functional group type. Instead, variations in resin structure, including polymer matrix composition, porosity, degree of cross-linking, and accessibility of exchange sites, are likely to play a critical role in governing phosphate sorption behaviour (Wang et al., 2023, Yin et al., 2024, Marin et al., 2024).

A comparison of the isotherm obtained in this study with those reported in previous investigations using FerrIX A33E reveals both agreement and notable discrepancies. The isotherm derived in the present work shows good consistency with that reported by Li et al. (2020), indicating comparable phosphate uptake behaviour under similar experimental conditions. In contrast, the isotherm reported by Nur et al. (2014a) exhibits substantially higher sorption capacities than those observed in both this study and that of Li et al. (2020). Given that key experimental conditions, such as the initial phosphate concentration range, solution pH, solid-to-liquid ratio, temperature, and equilibrium time, are broadly comparable across the studies, the observed divergence is more likely attributable to differences in resin pre-treatment procedures, particle size distribution, and the analytical methods used for phosphate quantification and concentration calculations. Additionally, variations in data interpretation and isotherm fitting approaches may have contributed to the higher apparent capacities reported by Nur et al. (2014a). These observations highlight the sensitivity of phosphate isotherm parameters of FerrIX A33E to experimental design and the importance of standardised testing conditions when comparing sorption capacities across studies.

Table 2. Isotherm model equations and their parameters for phosphate sorption onto FerrIX A33E resin

Model	Equation	Parameter	Value	
Langmuir	$q_e = \frac{q_m K_L C_e}{1 + K_L C_e}$	K_L (L/mg P)	1.480	(3)
		q_m (mg P/g)	6.362	
		R^2	0.991	
Freundlich	$q_e = K_f C_e^{\frac{1}{n}}$	K_f ($mg^{1-1/n}.L^{1/n}/g$)	3.621	(4)
		n (-)	4.556	
		R^2	0.999	
Dubinin-Radushkevich	$q_e = q_m \exp(-\beta\varepsilon^2)$	β (mol^2/kJ^2)	9.5×10^{-8}	(5)
	$\varepsilon = RTln(1 + \frac{1}{C_e})$	q_m (mg P/g)	5.71	(6)
		R^2	0.979	
Redlich-Peterson	$q_e = \frac{K_R C_e}{1 + a_R C_e^{\beta}}$	K_R (L/mg P)	1.9×10^4	(7)
		a_R (L^{β}/mg^{β})	5.2×10^3	
		β (-)	0.781	
		R^2	0.999	

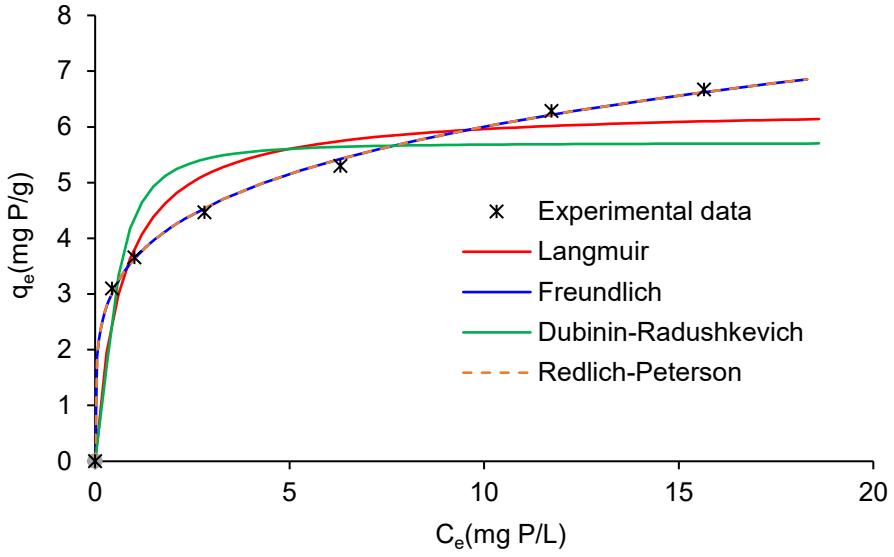

Figure 3. Isotherm models for the sorption of phosphate onto FerrIX A33E resin (T=20°C)

Table 3: Comparison of isotherm parameters obtained in this study with previous studies for phosphate removal

Resin	Model	Parameters*	R^2	Reference
Lewatit Monoplus M 600	Langmuir	Q_m = 9.49 K_L = 1.53	0.84	(Bektaş et al., 2021)
Lewatit Monoplus M 600	Freundlich	K_F = 5.70 1/n = 0.565	0.94	(Bektaş et al., 2021)
Purolite A200E	Langmuir	Q_m = 53.045 K_L = 0.2678	0.82	(Korkmaz et al., 2023)
Purolite A200E	Freundlich	K_F = 18.439 1/n = 0.2365	0.99	(Korkmaz et al., 2023)
AMBERLITE HPR9200	Langmuir	Q_m = 13.16 K_L = 1.10	0.98	(Li et al., 2020)
AMBERLITE HPR9200	Freundlich	K_F = 1.12 1/n = 0.694	0.99	(Li et al., 2020)
FerrIX 33E	Langmuir	Q_m = 7.69 K_L = 7.29	0.99	(Li et al., 2020)
FerrIX 33E	Freundlich	K_F = 3.76 1/n = 0.226	0.99	(Li et al., 2020)
FerrIX A33E	Langmuir	Q_m = 35.4 K_L = 0.22	0.95	(Nur et al., 2014a)
FerrIX A33E	Freundlich	K_F = 6.07 1/n = 0.64	0.95	(Nur et al., 2014a)
FerrIX A33E	Freundlich	K_F = 3.621 1/n = 0.2195	0.99	This study

*: The above parameters assume that C_e is in mg P/L and q_e is in mg P/g resin.

Based on the isotherm analysis, which was best described by the Freundlich model, the sorption mechanism appears to be non-ideal and deviates from classical monolayer ion exchange behaviour, indicating heterogeneous surface interactions and multiple binding sites. This could be attributed to the presence of iron oxide nanoparticles embedded within the FerrIX A33E resin structure. The results suggest that phosphate removal is not governed solely by conventional ion exchange but rather involves additional uptake mechanisms. Indeed, previous studies have demonstrated that ion exchange may account for only a minor fraction (~10%) of the overall phosphate removal capacity of ferric nanoparticle-embedded media, with up to 90% of uptake attributed to adsorption onto the ferric component of the resin (Martin et al., 2013). Phosphate adsorption via strong surface complexation on iron oxide nanoparticles, driven by

the high ligand affinity of phosphate for iron, therefore represents a dominant and critical removal mechanism (Smith et al., 2008, Spiteri et al., 2008). Accordingly, phosphate removal by FerrIX A33E is governed by a dual mechanism, involving conventional anion exchange at the quaternary ammonium group ($[NR4]^+$) alongside selective sorption and surface complexation on the hydrated ferric oxide sites (≡FeOH) embedded within the resin matrix. Within the pH range of the study (6 to 8), the phosphate species are $H_2PO_4^-$ and HPO_4^{2-} (Fig S2 – Supplementary Information). Equations 8 and 9 describe the exchange of the phosphate species with the quaternary amine groups of the resin while Equations 10 and 11 describe the sorption/complexation with ferric particles. Since the point of zero charge (PZC) of hydrated iron oxides is around 7.9 (Ownby et al., 2021), pH plays an important role regarding the interaction between phosphates and the iron oxides. Therefore, lower pH values than PZC=7.9, which is typical in water treatment, favours phosphates removal from water while higher pH than 7.9 deprotonates the iron oxides to FeO^- favouring the release of phosphates into solution. Figure 4 provides a schematic showing the dual mechanisms for phosphates removal by ion exchange and sorption/complexation in ferric oxides of both monovalent and divalent phosphate ions (i.e. $H_2PO_4^-$ and HPO_4^{2-}).

$$-NR_4^+Cl^- + H_2PO_4^- \leftrightarrow -NR_4.H_2PO_4 + Cl^- \quad (8)$$

$$2(-NR_4^+Cl^-) + HPO_4^{2-} \leftrightarrow (-NR_4)_2.HPO_4 + 2Cl^- \quad (9)$$

$$(\equiv FeOH_2^+) + H_2PO_4^- \leftrightarrow (\equiv FeOH_2^+).H_2PO_4 \quad (10)$$

$$2(\equiv FeOH_2^+) + HPO_4^{2-} \leftrightarrow (2(\equiv FeOH_2^+)).HPO_4 \quad (11)$$

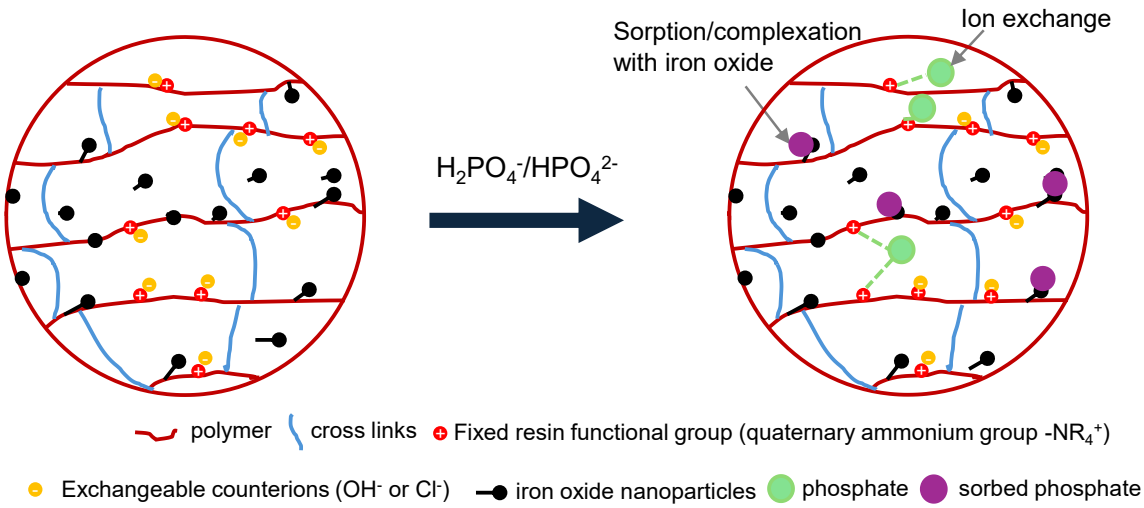

Figure 4. Dual mechanisms for phosphate removal by FerrIX A33E (ion exchange with the counter ions and adsorption/complexation with iron oxides).

3.3 Kinetics of phosphate uptake

In batch studies, kinetic experiments help determining the contact time required to reach equilibrium (Helfferich, 1995, Slater, 1991). High-speed mixing generates intense turbulence around the resin particles, reducing external liquid-film mass transfer resistance and shifting the rate-limiting step of mass transfer toward intraparticle diffusion. Accordingly, the kinetics of phosphate removal by FerrIX A33E were tested at different mixing speeds and analysed using several kinetic models, including the first-order reversible, Elovich, and particle diffusion models. The governing equations for these models are summarised in Table 4.

405 *Table 4. Kinetic models used to describe phosphate sorption onto FerrIX A33E*

Model	Equation	
Elovich	$q_t = \left(\frac{1}{b}\right)\ln(ab) + \left(\frac{1}{b}\right)\ln(t)$	(12)
First-order	$\ln[1 - U(t)] = -kt$	(13)
reversible	$U(t) = \frac{C_{Ao} - C_A}{C_{Ao} - C_{Ae}}$	(14)
Particle diffusion	$U(\tau) = [1 - \exp(\pi^2(f_1(\alpha)\tau + f_2(\alpha)\tau^2 + f_3(\alpha)\tau^3)]^{\frac{1}{2}}$	(15)
	$\tau = \frac{\bar{D}_a.t}{r_o^2}$	(16)
	$\frac{1}{f_1(\alpha)} = -0.570 - 0.430\alpha^{0.775}$	(17)
	$\frac{1}{f_2(\alpha)} = 0.260 + 7.82\alpha$	(18)
	$\frac{1}{f_3(\alpha)} = -0.165 - 0.117\alpha$	(19)

406

407 The kinetic experiments showed that equilibrium was achieved within approximately 50
408 minutes under high-speed mixing (150 rpm), whereas more than 90 minutes were required to
409 reach equilibrium at low-speed mixing (30 rpm), as illustrated in Figure 5. Fitting of the
410 experimental data to the kinetic models (Figure 5) indicates that the reversible first-order and
411 particle diffusion models provide the best representation of the data under high-speed mixing
412 conditions, whereas the Elovich model is more suitable at low mixing speeds. These findings
413 suggest that mixing speed strongly influences both the kinetics and the dominant mass transfer
414 mechanisms. In ion exchange systems, the rate-controlling step is typically governed by
415 resistance in the external liquid film, intraparticle diffusion, or a combination of both. As
416 mixing speed increases, the thickness of the mass transfer film surrounding the resin particles
417 decreases, enhancing film diffusion and shifting the rate-limiting step toward intraparticle
418 diffusion. This transition explains why the particle diffusion model provides a good fit to the

experimental data at high mixing speed (Figure 5a). At low mixing speed (Figure 5b), the first-order model adequately describes the initial uptake phase (t<30 min), consistent with the linear rate model associated with external film diffusion control (Brandani, 2021). It should be noted that, in addition to mixing speed, film diffusion commonly dominates the rate-determining step when the solute concentration in the liquid phase is low or when the resin possesses a high exchange capacity. Overall, the kinetic data at low mixing speed were best described by the Elovich equation, a model widely used to represent activated chemisorption processes (Aharoni and Tompkins, 1970, Juang and Chen, 1997). The Elovich model assumes that the sorption rate decreases exponentially with time as surface coverage increases, reflecting the progressive occupation of energetically heterogeneous sites. The good agreement between the Elovich model and the experimental data further supports the involvement of chemical interactions in phosphate uptake by FerrIX A33E, consistent with sorption on a heterogeneous surface as demonstrated by the isotherm analysis and the proposed removal mechanisms (Figure 4).

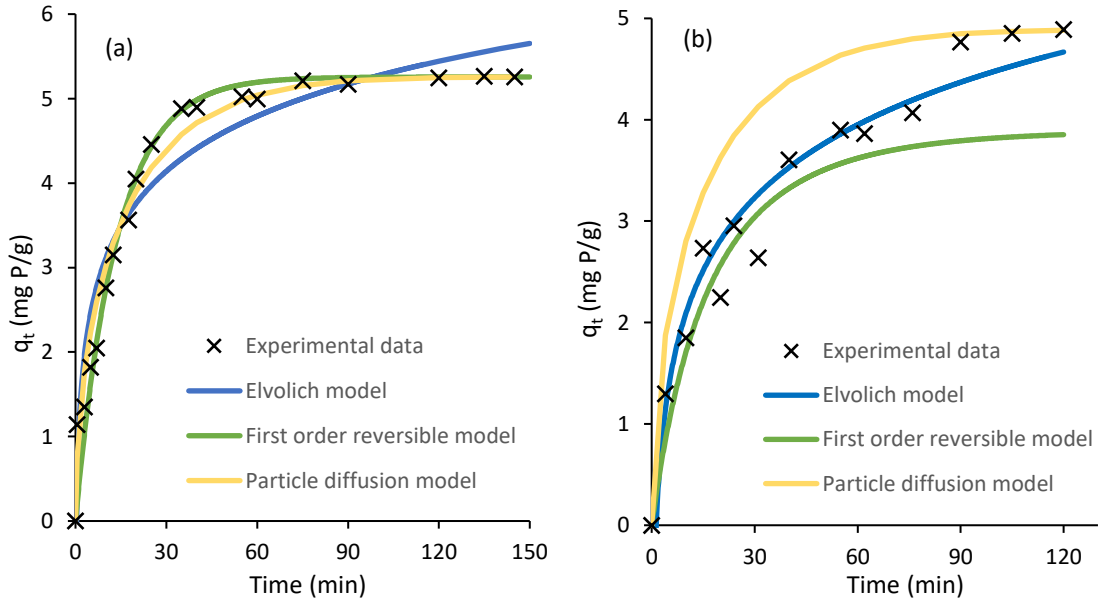

Figure 5. Kinetic models for the sorption of phosphate onto FerrIX A33E resin at different mixing speeds (a) 150 rpm, (b) 30 rpm

3.4 Column Breakthrough results

3.4.1 Breakthrough models

The successful design of an ion exchange column requires precise prediction of contaminant breakthrough during operation (Chittoo and Sutherland, 2020, Cheng and Knappe, 2024). Accordingly, phosphate uptake by the FerrIX A33E resin was studied under fixed-bed column conditions, and the results are presented as breakthrough curves. These curves plot the normalised phosphate concentration in the effluent, expressed as the ratio of effluent (C_t) to influent (C_0) concentration ($x_b = C_t/C_0$) versus time (t). The factors investigated for their impact on the breakthrough behaviour included bed height, influent flow rate, and the phosphate concentration of the feed solution (C_0). The resulting breakthrough curves were then analysed using several models, including the Bohart-Adams, Thomas, Clark and two modified Bohart-Adams variants: the *n*-order and fractal B-A models respectively (Hu et al., 2021, Bibiano-Cruz et al., 2016, Mestri et al., 2023). A summary of the equations governing these breakthrough curve models is given in Table 5.

Table 5. Mathematical models used to describe the breakthrough curves

Model	Equation	
Bohart-Adams (BAM)	$\frac{C_t}{C_o} = \frac{e^{\tau}}{(e^{\beta} - 1 + e^{\tau})}$	(20)
	$\beta = \frac{k_{BA}\rho_P q_0 Z}{v}\left(\frac{1-\varepsilon}{\varepsilon}\right)$	
	$\tau = k_{BA}C_o\left(t - \frac{Z}{v}\right)$	
Thomas (TM)	$\ln\left(\frac{C_o}{C_t} - 1\right) = \frac{k_{Th}q_{ads}m}{Q} - k_{Th}C_o t$	(21)

Clark (CM)

$$\frac{C_t}{C_0} = \left(\frac{1}{1 + Ae^{-rt}}\right)^{\frac{1}{n-1}} \quad (22)$$

$$A = \left(\frac{C_o^{n-1}}{C_b^{n-1}} - 1\right) e^{rt_b} \quad (23)$$

B-A n Order (n-BAM)

$$\frac{C_t}{C_0} = 1/\left[1 + n{a_0}^{1-n}{c_0}^{n-1}\left(\left[\frac{1 + (n-1)k_n{a_0}{c_0}^{n-1}x}{1 + (n-1)k_n{a_0}^{n-1}c_0 t}\right]^{\frac{1}{n-1}} - \left[\frac{1}{1 + (n-1)k_n{a_0}^{n-1}c_0 t}\right]^{\frac{1}{n-1}}\right)\right]^{\frac{1}{n}} \quad (24)$$

B-A Fractal (f-BAM)

$$\frac{C_t}{C_0} = \frac{\exp\left(\frac{1}{1-h}k_{BA,0}t^{1-h}c_0\right)}{\exp\left(\frac{k_{BA,0}t^h a_0 x}{u}\right) + \exp\left(\frac{1}{1-h}k_{BA,0}t^{1-h}c_0\right) - 1} \quad (25)$$

3.4.2 Effect of flow rate

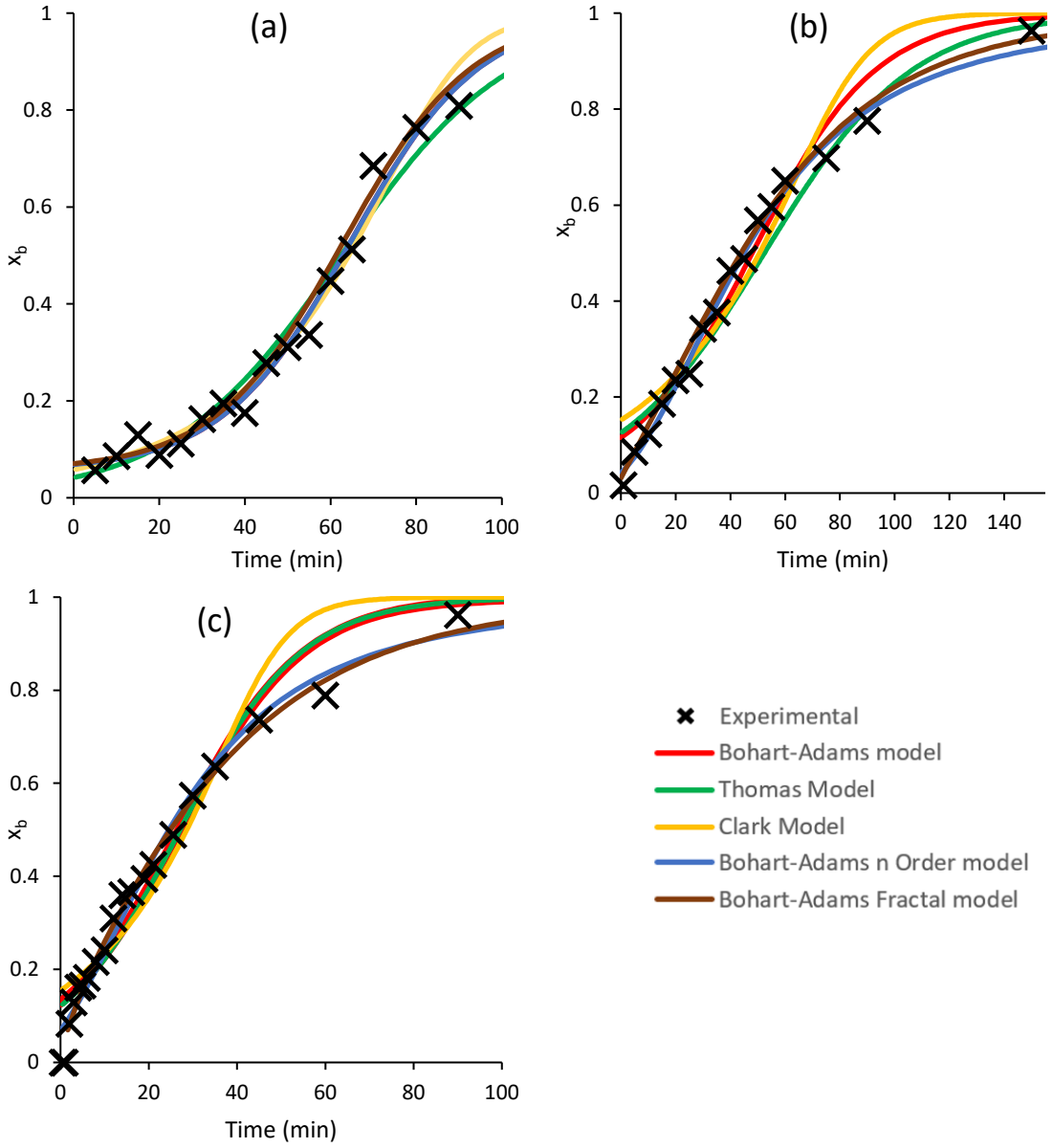

Figure 6. Breakthrough curves measured at different flow rates (a) 30 mL/min (b) 60 mL/min and (c) 90 mL/min (bed height = 5cm, C_0 = 33.3 mg P/L; $x_b = C_t/C_0$)

Figure 6a-c shows the breakthrough curves measured at different flowrates (30, 60, and 90 mL/min), whilst the bed height and inlet concentration were kept constant at 5cm and 33.3 mg P/L, respectively. As anticipated, the breakthrough occurred earlier when the flowrate was high due to the low contact time between the fluid and the resin particles. As shown in Figure 6 and at the lowest flowrate (30 mL/min), the breakthrough occurred at ~30 minutes (Figure 6a)

whilst when the flowrate was increased to 60 and 90 mL/min, the breakthroughs occurred almost instantly (Figure 6b & c). At the flowrate of 30 mL/min, all the five mathematical models described well the first half of the experimental data (i.e. $x_b < \sim 0.5$), but diverged at the endpoint of the breakthrough (Figure 6a). At high flow rates, Figure 6b-c shows that the BAM, TM, and CM models initially provide a reasonable fit to the experimental data but deviate significantly near the tail of the breakthrough curves, with the CM model showing the poorest agreement. In contrast, the *n*-order and fractal BAM models consistently offered the best fit to the experimental data across all flow rates tested. Table S1 (Supplementary Information) shows the parameters calculated for each model. As shown in Table S1 (Experiments 1-3), increasing the flow rate resulted in higher mass transfer rate constants across all models, consistent with previous findings that external film resistance plays a significant role in controlling the rate of phosphate uptake. Table S1 (Experiments 1-3) further indicates that flow rate also influenced the resin capacity (q_0), likely due to phosphate ions passing through the column too rapidly to achieve full contact with the resin particles.

3.4.3 Effect of inlet phosphate concentration

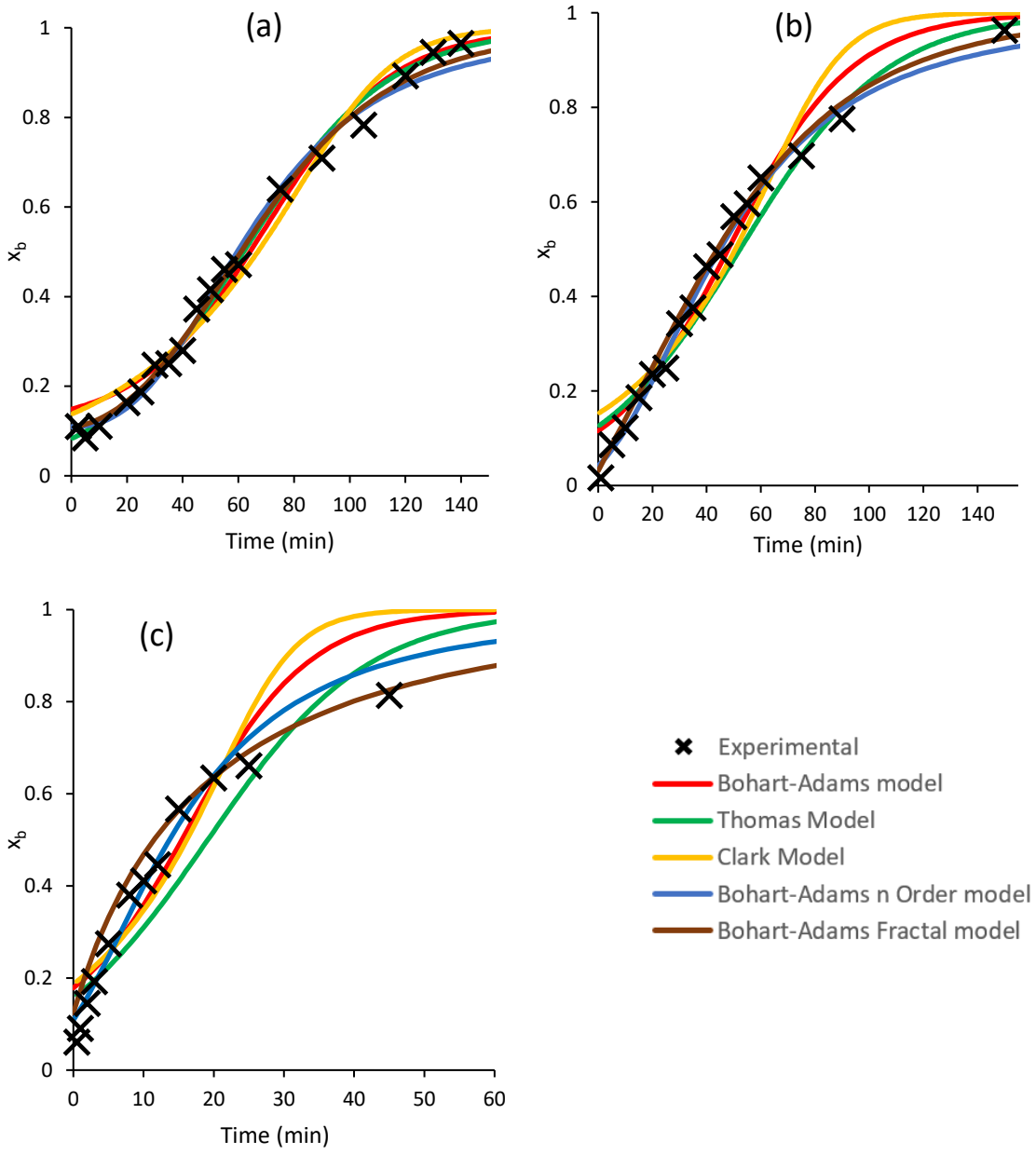

Figure 7. Breakthrough curves at different inlet concentrations (5cm bed depth and 60 mL/min) (a) 16.7 mg P/L (b) 33.3 mg P/L and (c) 66.7 mg P/L

Figure 7 shows the breakthrough curves at different inlet phosphate concentrations (16.7, 33.3, and 66.7 mg P/L), while the bed height and flowrate were set at 5 cm and 60 mL/min, respectively. According to Figure 7, the breakthrough occurred earlier when the inlet phosphate concentration was high, which is consistent with other studies (Nur et al., 2014a). Figure 7a illustrates that all models showed good agreement with the experimental data at the lowest

492 phosphate concentration. However, as the influent phosphate concentration increased, most
493 models deviated from the experimental results, with the exception of the n-order BAM (*n*-
494 BAM) and fractal BAM (*f*-BAM) models, which maintained strong predictive accuracy, as
495 reflected in their corresponding R^2 values (Table S1). This behaviour arises because the BAM,
496 TM, and CM models are primarly suited for symmetrical breakthrough curves, whereas the n-
497 BAM and f-BAM models can accurately capture the asymmetry observed in the breakthrough
498 curves, as seen in Figures 7b and 7c. Additionally, both the Bohart-Adams and Thomas models
499 assume that the surface reaction is the rate-limiting step, meaning that the constants k_{Th} and k_{AB}
500 do not represent the intrinsic rate of the process. Significant deviations between model
501 predictions and experimental data can therefore arise when particle diffusion, rather than
502 surface reaction, controls the overall rate (Chu, 2010). Consequently, the observed kinetics
503 likely result from the combined effects of surface reaction and intraparticle diffusion (Chu,
504 2010). The limitation of the Clark model is related to the assumption that the mass-transfer
505 coefficient is constant, which may not be suitable for a heterogeneous diffusion limited process
506 (Hu et al., 2020). At the highest phosphate concentration, the f-BAM model outperformed all
507 other models, demonstrating its superior ability to describe phosphate uptake by FerrIX A33E
508 across the full range of concentrations studied. This highlights the robsutness of the f-BAM
509 model for representing the phosphate-FerrIX A33E system, particularly due to its capacity to
510 account for diffusion-limited processes and surface heterogeneity. Table S1 (Experiments 2, 4,
511 and 5) summarises the f-BAM parameters calculated for the different influent concentrations.
512 A notable feature of the f-BAM model is that its rate coefficient, k_{BA} (expressed as $k_{BA}=k_{BA,0}t^{-h}$
513 , with $0 \leq h \leq 1$), incorporates a temporal "memory" effect and therefore is not constant over
514 time (Kopelman, 1988).

515

516 3.4.4 Effect of bed height

517

518

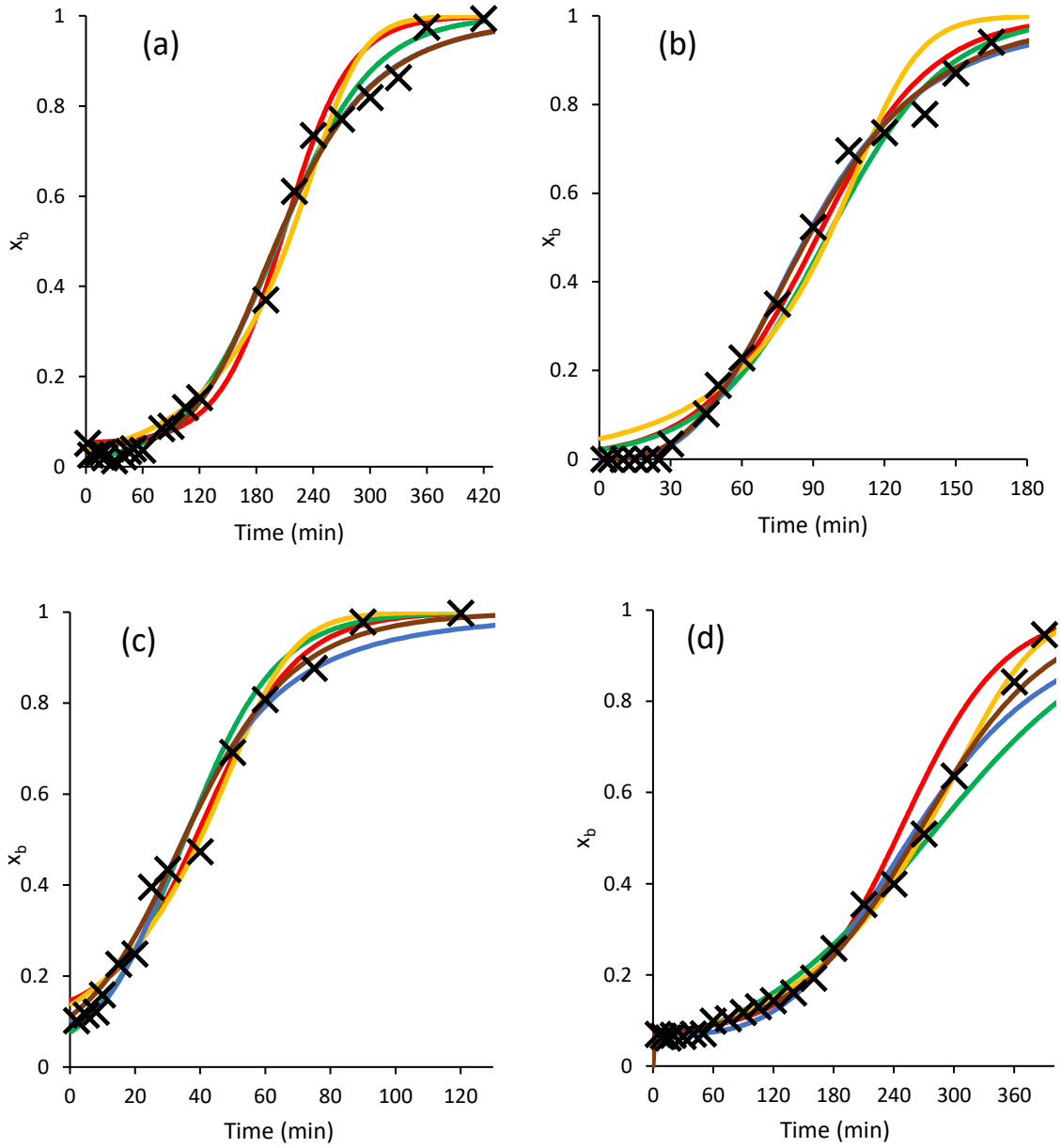

519

520

521

522

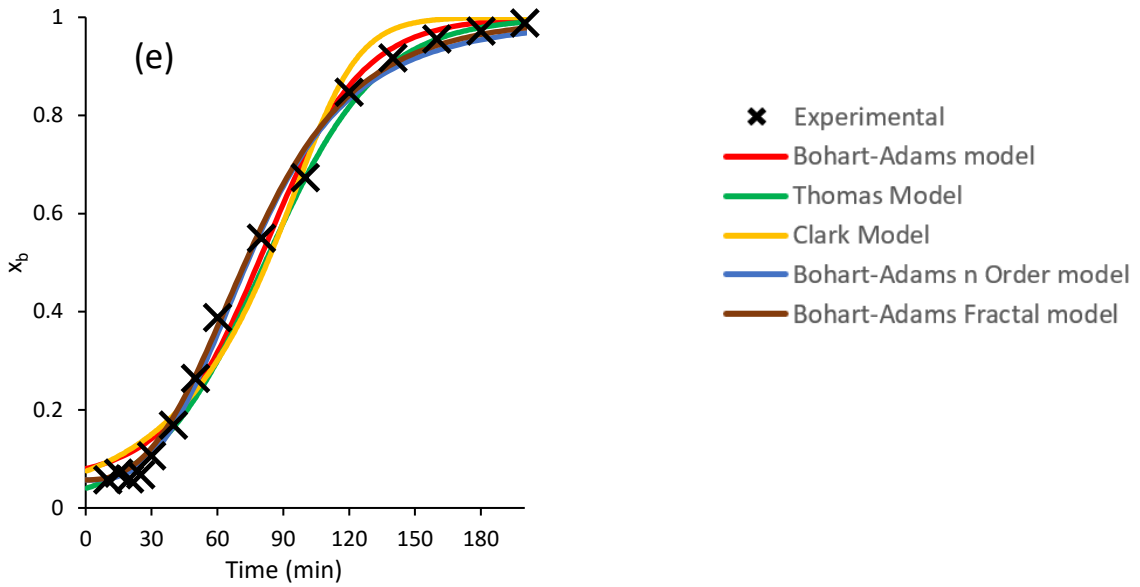

Figure 8. Breakthrough curves at 10 cm bed hight and: (a) 30 mL/min, 33.3 mg P/L (b) 60 mL/min, 33.3 mg P/L (c) 120 mL/min, 33.3 mg P/L, (d) 60 mL/min, 16.7 mg P/L, and (e) 60 mL/min, 66.7 mg P/L

To evaluate the effect of bed height, experiments at a bed height twice that used previously (i.e. 10 cm) were carried out at different flow rates and different inlet concentrations (Figure 8). As can be observed when comparing the breakthrough results shown in Figure 8 (a,b,c) vs Figure 6 (a,b,c) (i.e. constant inlet phosphate concentration and variable flow rate), the doubling of the bed height resulted in significant increase in breakthrough time (t_b). For example, at a flow rate of 30 mL/min, t_b increased from 30 min to 120 min as the bed height increased from 5 to 10 cm. Similarly, for experiments carried out at constant flow rate but variable inlet concentration, the increase of bed height also increased t_b (Figure 7(a,b,c) vs Figure 8(d,b,e)) and Table S1. Calculation of the difference in the values of t_b at 10 cm and 5 cm bed heights (Δt_b) shows that Δt_b is inversely proportional to the flow rate and to the inlet phosphate concentration with slopes of -1.47 min/(mL/min) and -0.24 min/(mg P/L).

The breakthrough curves for a bed height of 10 cm were also modelled, with the results presented in Figure 8. Overall, the figure demonstrates that at the greatest bed height, deviations

between the model predictions and experimental data were less pronounced compared to those observed at the smaller bed height. Nevertheless, the quality of the model fits was still influenced by variations in influent concentration and flow rate, similar to the trends observed for the shorter bed. Figure 8(d, b, e) shows that while all models fitted well the experimental data during the initial phase of the breakthrough curves, the BAM, CM, and TM models diverged near the curve tails, approaching equlibrium. Both the n-BAM and f-BAM models provided a strong fit across the entire breakthrough profile, though the n-BAM model exhibited a slight departure from the experimental data compared to f-BAM. These results further demonstrate that the f-BAM model consistently offers the most accurate representation of the experimental data, even at increased bed heights.

Overall, the BAM, CM, and TM models perfromed poorly under conditions of high phosphate concentrations, elevated flow rates, or low bed heights, largely due to the asymmetrical shape of the resulting breakthrough curves. In contrast, the fit of all models improved markedly when the bed height was increased from 5 cm to 10 cm. The asymmetry observed in the breakthrough curves may arise from variations in sorption mechanisms, surface heterogeneity, shifts in the rate-limiting step, and non-uniform flow distribution within the column. Consequently, the n-BAM and f-BAM models provided the best fits of the experimental data, as they account for both the dynamic behaviour and the asymmetric nature of the breakthrough curves. The dynamic model f-BAM outperformed n-BAM, owing to the time-dependency of its rate coefficient, and was therefore considered the most suitable model for decsribing the breakthrough curves of phosphate uptake by FerrIX A33E resin.

3.5 Regeneration

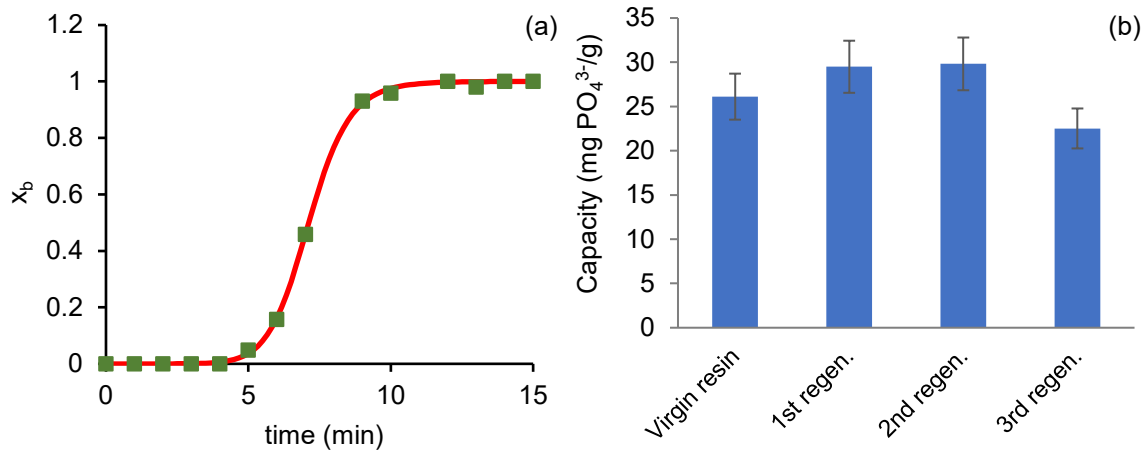

Figure 9. (a) Breakthrough curve for resin regeneration using a 5% sodium chloride solution (symbols represent experimental data; the solid red line denotes the f-BAM model fit with the parameters: $h = 0.271$; $k_{BA,0} = 0.035$ L.mg.min^{h-1}; $a_0 = 965.4$ mg P/L), (b) effect of repeated regeneration

To avoid the use of acids, a 5% sodium chloride solution was used as the regenerant at a flow rate of 30 mL/min. The resin bed length was 10 cm. Following the initial sorption run with virgin resin, the sorption-regeneration cycle was repeated three times. Each sorption cycle was conducted using an influent phosphate concentration of 100 mg P/L at a flow rate of 60 mL/min. Figure 9(a) shows that chloride breakthrough occurred at around 5 minutes, while complete resin regeneration was achieved at about 10 minutes. The experimental data are well described by the f-BAM model, demonstrating excellent agreement between measured and predicted behaviour (Figure 9(a)).

For any loading or regeneration breakthrough curve, the average resin composition along the bed and the total resin capacity can be estimated by integrating the area above the breakthrough curve (Slater, 1991).

Figure 9(b) presents the evolution of resin capacity, calculated by integrating the breakthrough curves, over successive regeneration cycles. Notably, the average capacity after the first regeneration (Figure 9(b)) is slightly higher than that of the virgin resin, suggesting that initial operation may activate or expose additional sorption sites, thereby enhancing the effective capacity of the resin. The first and the second regeneration runs show very similar capacities, but after the third regeneration cycle, the average resin capacity slightly decreased by ~14%, though it remained within the experimental error of the resin capacity (Figure 9(b) error bars). This finding suggests that FerrIX A33E is a promising material for both the effective removal and potential recovery of phosphates from water. Its dual functionality supports not only compliance with stringent discharge regulations but also aligns with circular economy principles. By mitigating phosphate-induced eutrophication, the resin offers a sustainable approach to protecting aquatic ecosystems against the adverse environmental effects of excessive nutrient enrichment.

Conclusions

This study demonstrated that FerrIX A33E is effective for the removal of phosphates from water. Both ion exchange and removal via sorption or complex formation with iron oxide nanoparticles were suggested as key mechanisms governing phosphate uptake by FerrIX A33E. Isotherm analysis showed that the Redlich-Peterson and Freundlich models provided a superior fit to the experimental data compared with the Langmuir and Dubinin-Radushkevich models, indicating a heterogeneous resin surface. This heterogeneity is likely associated with the

presence of iron-based ionogenic groups and multiple reactive sites contributing to phosphate binding.

The kinetic studies revealed that mixing speed influences the mechanisms governing phosphate uptake by FerrIX A33E resin. The Elovich model adequately described the kinetic experimental data across all mixing speeds, indicating the involvement of chemisorption on a heterogeneous surface, whereas the particle diffusion model provided a good fit only at high mixing speeds, where intraparticle diffusion became the dominant rate-limiting step. The breakthrough curve analysis from the dynamic column experiments showed that models capable of describing asymmetric breakthrough curves, namely the n-order Bohart-Adams and fractal Bohart-Adams models, provided superior fits to the experimental data. These models consistently outperformed the conventional Bohart-Adams, Thomas, and Clark models, which are inherently limited to symmetric breakthrough curves and therefore failed to accurately capture the observed column behaviour.

Repeated use of the FerrIX A33E resin did not result in a significant loss of phosphate uptake capacity, indicating good stability and reusability. These findings suggest that FerrIX A33E has strong potential as a sustainable option for phosphate removal and recovery, particularly if its performance is confirmed at larger scales and under realistic conditions using real wastewater effluents.

Supplementary Information The online version contains supplementary material available at xxxx.

627 **References**

628 ACELAS, N. Y., MARTIN, B. D., LÓPEZ, D. & JEFFERSON, B. 2015. Selective removal
629 of phosphate from wastewater using hydrated metal oxides dispersed within anionic
630 exchange media. *Chemosphere,* 119**,** 1353-1360.
631 AHARONI, C. & TOMPKINS, F. C. 1970. Kinetics of Adsorption and Desorption and the
632 Elovich Equation. *In:* ELEY, D. D., PINES, H. & WEISZ, P. B. (eds.) *Advances in*
633 *Catalysis.* Academic Press.
634 ALMASRI, D. A., SALEH, N. B., ATIEH, M. A., MCKAY, G. & AHZI, S. 2019.
635 Adsorption of phosphate on iron oxide doped halloysite nanotubes. *Scientific Reports,*
636 9**,** 3232.
637 AWUAL, M. R. 2019. Efficient phosphate removal from water for controlling eutrophication
638 using novel composite adsorbent. *Journal of Cleaner Production,* 228**,** 1311-1319.
639 BEKTAŞ, T. E., UĞURLUOĞLU, B. K. & TAN, B. 2021. Phosphate removal by Ion
640 exchange in batch mode. *Water Practice and Technology,* 16**,** 1343-1354.
641 BIBIANO-CRUZ, L., GARFIAS, J., SALAS-GARCÍA, J., MARTEL, R. & LLANOS, H.
642 2016. Batch and column test analyses for hardness removal using natural and
643 homoionic clinoptilolite: breakthrough experiments and modeling. *Sustainable Water*
644 *Resources Management,* 2**,** 183-197.
645 BLANEY, L. M., CINAR, S. & SENGUPTA, A. K. 2007. Hybrid anion exchanger for trace
646 phosphate removal from water and wastewater. *Water Research,* 41**,** 1603-1613.
647 BOL, R., GRUAU, G., MELLANDER, P.-E., DUPAS, R., BECHMANN, M.,
648 SKARBØVIK, E., BIEROZA, M., DJODJIC, F., GLENDELL, M., JORDAN, P.,
649 VAN DER GRIFT, B., RODE, M., SMOLDERS, E., VERBEECK, M., GU, S.,
650 KLUMPP, E., POHLE, I., FRESNE, M. & GASCUEL-ODOUX, C. 2018. Challenges

651 of Reducing Phosphorus Based Water Eutrophication in the Agricultural Landscapes
652 of Northwest Europe. *Frontiers in Marine Science,* Volume 5 - 2018.
653 BRANDANI, S. 2021. Kinetics of liquid phase batch adsorption experiments. *Adsorption,* 27**,**
654 353-368.
655 CARPENTER, S. R., CARACO, N. F., CORRELL, D. L., HOWARTH, R. W., SHARPLEY,
656 A. N. & SMITH, V. H. 1998. Nonpoint Pollution of Surface Waters with Phosphorus
657 and Nitrogen. *Ecological Applications,* 8**,** 559-568.
658 CHENG, L. & KNAPPE, D. R. U. 2024. Removal of Per- and Polyfluoroalkyl substances by
659 anion exchange resins: Scale-up of rapid small-scale column test data. *Water*
660 *Research,* 249**,** 120956.
661 CHITTOO, B. S. & SUTHERLAND, C. 2020. Column breakthrough studies for the removal
662 and recovery of phosphate by lime-iron sludge: Modeling and optimization using
663 artificial neural network and adaptive neuro-fuzzy inference system. *Chinese Journal*
664 *of Chemical Engineering,* 28**,** 1847-1859.
665 CHU, K. H. 2010. Fixed bed sorption: Setting the record straight on the Bohart–Adams and
666 Thomas models. *Journal of Hazardous Materials,* 177**,** 1006-1012.
667 CROSS, K. M., LU, Y., ZHENG, T., ZHAN, J., MCPHERSON, G. & JOHN, V. 2009.
668 Chapter 24 - Water Decontamination Using Iron and Iron Oxide Nanoparticles. *In:*
669 SAVAGE, N., DIALLO, M., DUNCAN, J., STREET, A. & SUSTICH, R. (eds.)
670 *Nanotechnology Applications for Clean Water.* Boston: William Andrew Publishing.
671 DAS, J., PATRA, B. S., BALIARSINGH, N. & PARIDA, K. M. 2006. Adsorption of
672 phosphate by layered double hydroxides in aqueous solutions. *Applied Clay Science,*
673 32**,** 252-260.

DUDEK, S. & KOŁODYŃSKA, D. 2022. Arsenate removal on the iron oxide ion exchanger modified with Neodymium(III) ions. *Journal of Environmental Management,* 307**,** 114551.

ENVIRONMENT AGENCY. 2019. *Phosphorus and Freshwater Eutrophication Pressure Narrative. Available at: https://consult.environment-agency.gov.uk/environment-and-business/challenges-and-choices/user_uploads/phosphorus-pressure-rbmp-2021.pdf* [Online]. [Accessed].

ENVIRONMENT AGENCY. 2025. *Phosphorus and freshwater eutrophication: challenges for the water environment. Available at: https://www.gov.uk/government/publications/phosphorus-challenges-for-the-water-environment* [Online]. [Accessed].

FLORES, C. V., OBESO, J. L., HERRERA-ZUÑIGA, L., PERALTA, R. A., CAMPERO-DOMÍNGUEZ, J. I., MORALES-RUIZ, L., PORTILLO-VÉLEZ, N. S. & VALDIVIA-CORONA, J. C. 2026. Layered double hydroxides (LDH) materials for effective phosphate adsorption from aqueous solution. *RSC Sustainability*.

FOSTER, X., TARPEH, W. A., DONG, H. & VANEECKHAUTE, C. 2025. Enhancing the regeneration efficiency of a hybrid anion exchange resin for removal of phosphorus from wastewater with a lower environmental impact. *Journal of Water Process Engineering,* 69**,** 106851.

GOH, K.-H., LIM, T.-T. & DONG, Z. 2008. Application of layered double hydroxides for removal of oxyanions: A review. *Water Research,* 42**,** 1343-1368.

GONZALEZ-PECH, N. I., MOLLOY, A. L., ZAMBRANO, A., LIN, W., BOHLOUL, A., ZARATE-ARAIZA, R., AVENDANO, C. & COLVIN, V. L. 2022. Feasibility of iron-based sorbents for arsenic removal from groundwater. *Journal of Chemical Technology & Biotechnology,* 97**,** 3024-3034.

699 GUIDA, S., RUBERTELLI, G., JEFFERSON, B. & SOARES, A. 2021. Demonstration of
700 ion exchange technology for phosphorus removal and recovery from municipal
701 wastewater. *Chemical Engineering Journal,* 420**,** 129913.
702 HELFFERICH, F. G. 1995. *Ion exchange*, Courier Corporation.
703 HU, Q., LIU, H., ZHANG, Z. & PEI, X. 2020. Development of fractal-like Clark model in a
704 fixed-bed column. *Separation and Purification Technology,* 251**,** 117396.
705 HU, Q., PANG, S., WANG, D., YANG, Y. & LIU, H. 2021. Deeper Insights into the Bohart-
706 Adams Model in a Fixed-Bed Column. *J Phys Chem B,* 125**,** 8494-8501.
707 JUANG, R.-S. & CHEN, M.-L. 1997. Application of the Elovich Equation to the Kinetics of
708 Metal Sorption with Solvent-Impregnated Resins. *Industrial & Engineering*
709 *Chemistry Research,* 36**,** 813-820.
710 KOPELMAN, R. 1988. Fractal reaction kinetics. *Science,* 241**,** 1620-6.
711 KORKMAZ, C., DEĞERMENCI, G. D. & DEĞERMENCI, N. 2023. Removal of Phosphate
712 from Aqueous Solution Using Anion Exchange Resin: Equilibrium Isotherms and
713 Kinetics. *Fibers and Polymers,* 24**,** 3753-3760.
714 LI, R., WANG, J. J., ZHOU, B., AWASTHI, M. K., ALI, A., ZHANG, Z., GASTON, L. A.,
715 LAHORI, A. H. & MAHAR, A. 2016. Enhancing phosphate adsorption by Mg/Al
716 layered double hydroxide functionalized biochar with different Mg/Al ratios. *Science*
717 *of The Total Environment,* 559**,** 121-129.
718 LI, Z., XU, S., LI, Y. & ARAI, Y. 2020. Novel Application of Hybrid Anion Exchange Resin
719 for Phosphate Desorption Kinetics in Soils: Minimizing Re-Adsorption of Desorbed
720 Ions. *Soil Systems,* 4**,** 36.
721 LIU, R., CHI, L., WANG, X., SUI, Y., WANG, Y. & ARANDIYAN, H. 2018. Review of
722 metal (hydr)oxide and other adsorptive materials for phosphate removal from water.
723 *Journal of Environmental Chemical Engineering,* 6**,** 5269-5286.

LU, X., GUO, W., WANG, B., FENG, Y., HE, S. & XUE, L. 2023. Screening optimal preparation conditions of low-cost metal-modified biochar for phosphate adsorption and unraveling their influence on adsorption performance. *Journal of Cleaner Production,* 425**,** 138927.

LUO, D., WANG, L., NAN, H., CAO, Y., WANG, H., KUMAR, T. V. & WANG, C. 2023. Phosphorus adsorption by functionalized biochar: a review. *Environmental Chemistry Letters,* 21**,** 497-524.

MA, F. F., KANG, H. B., ZHAO, H., ZHENG, X. D., ZHANG, J., LI, Q. & JIAO, Y. X. 2025. Adsorption Mechanism of Phosphate on Layered Double Hydroxide-loaded Biochar and DFT Study. *Huan Jing Ke Xue,* 46**,** 4360-4369.

MANAWI, Y., HUSSIEN, M., BUEKENHOUDT, A., ZEKRI, A., AL-SULAITI, H., LAWLER, J. & KOCHKODAN, V. 2022. New ceramic membrane for Phosphate and oil removal. *Journal of Environmental Chemical Engineering,* 10**,** 106916.

MARIN, N. M., NITA LAZAR, M., POPA, M., GALAON, T. & PASCU, L. F. 2024. Current Trends in Development and Use of Polymeric Ion-Exchange Resins in Wastewater Treatment. *Materials,* 17**,** 5994.

MARTIN, B. D., DE KOCK, L., STEPHENSON, T., PARSONS, S. A. & JEFFERSON, B. 2013. The impact of contactor scale on a ferric nanoparticle adsorbent process for the removal of phosphorus from municipal wastewater. *Chemical Engineering Journal,* 215-216**,** 209-215.

MESTRI, S., DOGAN, S. & TIZAOUI, C. 2023. Bromate Removal from Water Using Ion Exchange Resin: Batch and Fixed Bed Column Performance. *Ozone: Science & Engineering,* 45**,** 291-304.

NUR, T., JOHIR, M. A. H., LOGANATHAN, P., NGUYEN, T., VIGNESWARAN, S. & KANDASAMY, J. 2014a. Phosphate removal from water using an iron oxide

749 impregnated strong base anion exchange resin. *Journal of Industrial and Engineering*
750 *Chemistry,* 20**,** 1301-1307.
751 NUR, T., SHIM, W. G., JOHIR, M. A. H., VIGNESWARAN, S. & KANDASAMY, J.
752 2014b. Modelling of phosphorus removal by ion-exchange resin (Purolite FerrIX
753 A33E) in fixed-bed column experiments. *Desalination and Water Treatment,* 52**,** 784-
754 790.
755 OWNBY, M., DESROSIERS, D.-A. & VANEECKHAUTE, C. 2021. Phosphorus removal
756 and recovery from wastewater via hybrid ion exchange nanotechnology: a study on
757 sustainable regeneration chemistries. *npj Clean Water,* 4**,** 6.
758 PUROLITE. 2021. *Arsenic removal for business and residential applications using FerrIX™*
759 *A33E. Available at: https://www.purolite.com/product/ferrixa33e* [Online].
760 [Accessed].
761 SENDROWSKI, A. & BOYER, T. H. 2013. Phosphate removal from urine using hybrid
762 anion exchange resin. *Desalination,* 322**,** 104-112.
763 SHOKRI, A. & SANAVI FARD, M. 2023. Principles, operational challenges, and
764 perspectives in boiler feedwater treatment process. *Environmental Advances,* 13**,**
765 100389.
766 SLATER, M. J. 1991. Chapter 3 - Kinetics of ion exchange in solution. *In:* SLATER, M. J.
767 (ed.) *Principles of Ion Exchange Technology.* Butterworth-Heinemann.
768 SMITH, S., TAKÁCS, I., MURTHY, S., DAIGGER, G. T. & SZABÓ, A. 2008. Phosphate
769 complexation model and its implications for chemical phosphorus removal. *Water*
770 *Environ Res,* 80**,** 428-38.
771 SPITERI, C., CAPPELLEN, P. V. & REGNIER, P. 2008. Surface complexation effects on
772 phosphate adsorption to ferric iron oxyhydroxides along pH and salinity gradients in
773 estuaries and coastal aquifers. *Geochimica et Cosmochimica Acta,* 72**,** 3431-3445.

774 THISTLETON, J., BERRY, T. A., PEARCE, P. & PARSONS, S. A. 2002. Mechanisms of
775 Chemical Phosphorus Removal II: Iron (III) Salts. *Process Safety and Environmental*
776 *Protection,* 80**,** 265-269.
777 THOMMES, M., KANEKO, K., NEIMARK, A. V., OLIVIER, J. P., RODRIGUEZ-
778 REINOSO, F., ROUQUEROL, J. & SING, K. S. W. 2015. Physisorption of gases,
779 with special reference to the evaluation of surface area and pore size distribution
780 (IUPAC Technical Report). *Pure and Applied Chemistry,* 87**,** 1051-1069.
781 THOMPSON, A. K., MATHWIG, K., FLETCHER, P. J., CASTAING, R. & MARKEN, F.
782 2021. Electroanalysis with a single microbead of phosphate binding resin (FerrIX™)
783 mounted in epoxy film. *Journal of Solid State Electrochemistry,* 25**,** 2881-2891.
784 USMAN, M. O., ATURAGABA, G., NTALE, M. & NYAKAIRU, G. W. 2022. A review of
785 adsorption techniques for removal of phosphates from wastewater. *Water Science and*
786 *Technology,* 86**,** 3113-3132.
787 WANG, B., HU, X., LI, L., XIE, Y., CHEN, R., GUO, W., WANG, H., WANG, M., SHI, J.,
788 CHEN, L. & ZHOU, D. 2023. Enhanced phosphate removal by filler encapsulation
789 and surface engineering using SA/PVA matrix: Fabrication optimization, adsorption
790 behaviors and inner removal mechanism. *Chemical Engineering Journal,* 472**,**
791 145073.
792 WANG, S.-X., HUANG, Y.-X., WU, Q.-F., YAO, W., LU, Y.-Y., HUANG, B.-C. & JIN, R.-
793 C. 2024. A review of the application of iron oxides for phosphorus removal and
794 recovery from wastewater. *Critical Reviews in Environmental Science and*
795 *Technology,* 54**,** 405-423.
796 YAN, Y., KALLIKAZAROU, N. I., NISIFOROU, O., SHANG, Q., FU, D., ANTONIOU,
797 M. G. & FOTIDIS, I. A. 2025. Phosphorus recovery through struvite crystallization

from real wastewater: Bridging gaps from lab to market. *Bioresource Technology,* 427**,** 132408.

YAO, Y., GAO, B., INYANG, M., ZIMMERMAN, A. R., CAO, X., PULLAMMANAPPALLIL, P. & YANG, L. 2011. Removal of phosphate from aqueous solution by biochar derived from anaerobically digested sugar beet tailings. *Journal of Hazardous Materials,* 190**,** 501-507.

YIN, T., LEI, Y., ZHANG, W., HUO, T., LIU, P., HUANG, Q., MANJORO, T. T. & DONG, F. 2024. Iron Monodentate Ligand Substituted Calcium Cross-Linking Gel Beads and Mechanism to Enhance Phosphate Adsorption. *Journal of Polymers and the Environment,* 32**,** 6320-6336.

YOON, S.-Y., LEE, C.-G., PARK, J.-A., KIM, J.-H., KIM, S.-B., LEE, S.-H. & CHOI, J.-W. 2014. Kinetic, equilibrium and thermodynamic studies for phosphate adsorption to magnetic iron oxide nanoparticles. *Chemical Engineering Journal,* 236**,** 341-347.

ZHANG, G., LIU, H., LIU, R. & QU, J. 2009. Removal of phosphate from water by a Fe–Mn binary oxide adsorbent. *Journal of Colloid and Interface Science,* 335**,** 168-174.

ZHANG, Y., XIAO, Y.-F., XU, G.-S., WANG, D.-C., LI, J., HUANG, J. & JIN, Z. 2023. Preparation of Fe2O3 porous microspheres modified pumice and its adsorption performance on phosphate removal. *Journal of Environmental Chemical Engineering,* 11**,** 109995.

Supplementary Information

Enhanced Phosphate Removal from Water Using Iron-Nanoparticle Impregnated Ion Exchange Resin (FerrIX A33E): Batch and Column Studies

Authors – Anonymised as requested by the journal

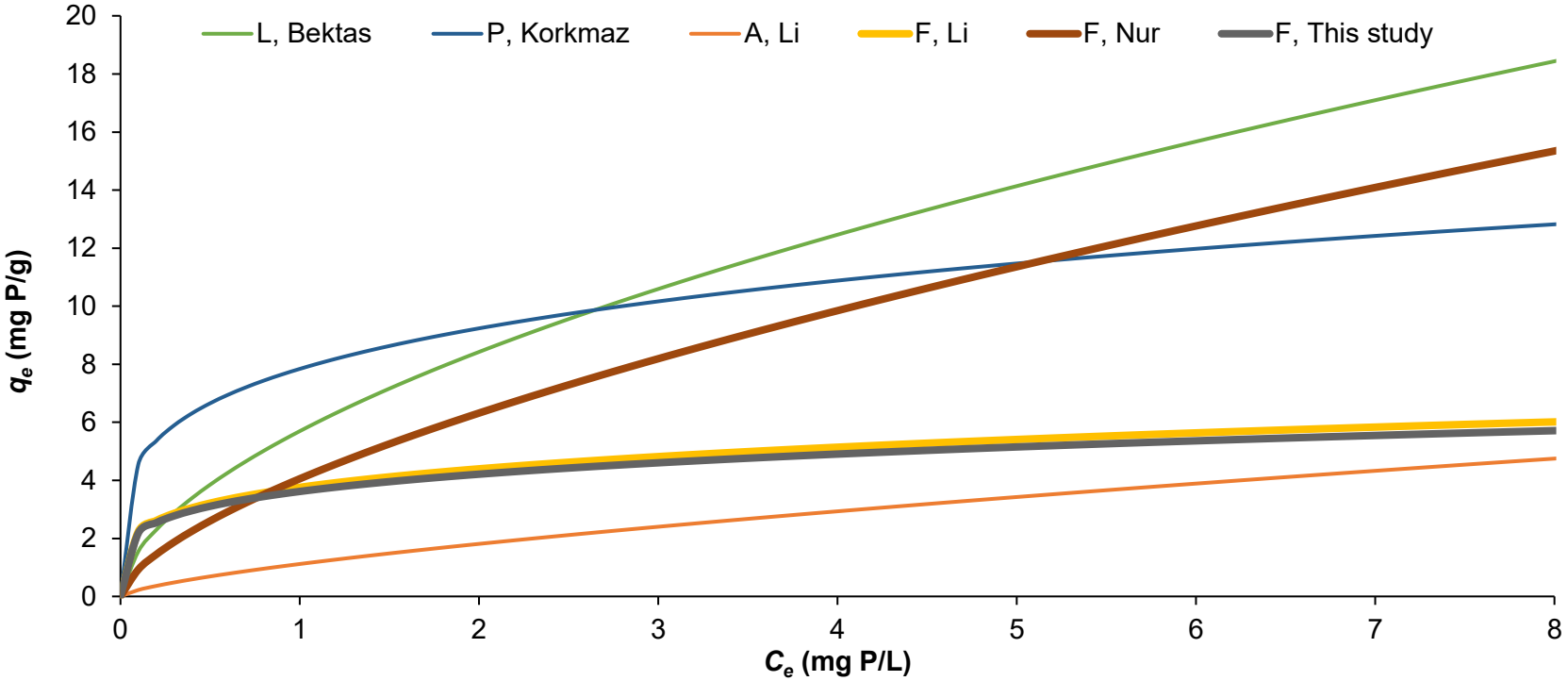

Figure S1: Comparison of different studies for phosphate ion exchange isotherms (thick lines are for FerrIX A33E)

A: AMBERLITE HPR9200; **F**: FerrIX A33E; **L**: Lewatit Monoplus M 600; **P**: Purolite A200E

Bektaş, T.E.; Uğurluoğlu, B.K.; Tan, B., Phosphate removal by ion exchange in batch mode. Water Practice and Technology 2021, 16, 1343-1354.
Korkmaz, C.; Değermenci, G.D.; Değermenci, N., Removal of phosphate from aqueous solution using anion exchange resin: Equilibrium isotherms and kinetics. Fibers and Polymers 2023, 24, 3753-3760.
Li, Z.; Xu, S.; Li, Y.; Arai, Y., Novel application of hybrid anion exchange resin for phosphate desorption kinetics in soils: Minimizing re-adsorption of desorbed ions. Soil Systems 2020, 4, 36.
Nur, T.; Johir, M.A.H.; Loganathan, P.; Nguyen, T.; Vigneswaran, S.; Kandasamy, J., Phosphate removal from water using an iron oxide impregnated strong base anion exchange resin. Journal of Industrial and Engineering Chemistry 2014, 20, 1301-1307.

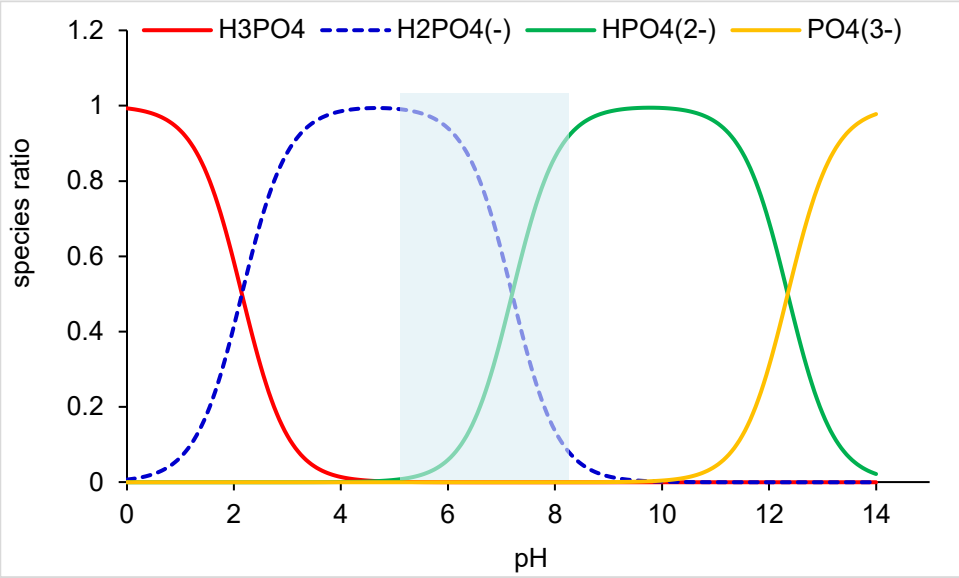

Figure S2. Phosphoric acid speciation

Table S1. Fitting parameters obtained from different breakthrough models

	Conditions			Bohart-Adams			Thomas Model			Clark Model			B-A n order				B-A fractal			
Exp.	**C_o (mg L^{-1})**	**Q (mL min^{-1})**	**Z (cm)**	k_{BA} (m^3 kg^{-1} s^{-1})	q_o (mg g^{-1})	R^2	k_{Th} (L mg^{-1} min^{-1})	q_o (mg g^{-1})	R^2	A (-)	r (min^{-1})	R^2	k_n (L^n $mg^{-n}min^{-1}$)	a_0 (mg L^{-1})	n (-)	R^2	k_{BA} (L mg^{-1} $min^{(h-1)}$)	a_0 (mg L^{-1})	h (-)	R^2
1	100.00	30.00	5.00	0.0111	24.6	0.96	5.03×10^{-5}	14.443	0.96	28509.71	0.1206	0.97	6.52×10^{-4}	2.48×10^{4}	1.0	0.97	0.67	2.42	0	0.96
2	100.00	60.00	5.00	0.0118	31.4	0.97	3.71×10^{-4}	20.96	0.90	2430.2	0.1336	0.95	1.17×10^{-6}	2.02×10^{8}	1.4	0.94	1.32	2.95	0.265	0.97
3	100.00	90.00	5.00	0.0129	34.8	0.92	7.32×10^{-4}	18.778	0.95	1151.70	0.1697	0.87	8.91×10^{-7}	2.50×10^{8}	1.4	0.89	1.38	2.73	0.239	0.92
4	200.00	60.00	5.00	0.0097	26.6	0.89	4.39×10^{-4}	17.694	0.79	621.02	0.1944	0.66	1.90×10^{-7}	1.39×10^{9}	1.5	0.84	1.43	1.87	0.425	0.88
5	50.00	60.00	5.00	0.0110	25.4	0.83	7.78×10^{-4}	14.272	0.98	2128.34	0.074	0.95	65.6	5.44×10^{5}	1.3	0.96	3.42	1.76	0.269	0.90
6	100.00	60.00	10.00	0.0071	37.0	0.91	4.02×10^{-4}	22.125	0.96	83366.35	0.0846	0.87	65.6	3.19×10^{5}	1.2	0.89	2.79	2.29	0.347	0.89
7	100.00	30.00	10.00	0.0048	39.9	0.94	2.02×10^{-4}	23.480	0.97	134597.72	0.044	0.93	65.6	2.23×10^{2}	1.2	0.93	3.84	2.17	0.443	0.94
8	100.00	120.00	10.00	0.0119	35.5	0.92	7.10×10^{-4}	16.274	0.97	1524.31	0.1106	0.96	65.6	6.90×10^{5}	1.3	0.90	1.59	2.37	0.189	0.92
9	200.00	60.00	10.00	0.0037	62.0	0.91	1.96×10^{-4}	37.774	0.99	17410.00	0.0733	0.92	65.6	5.81×10^{5}	1.2	0.94	1.45	3.79	0.349	0.92
10	50.00	60.00	10.00	0.0066	46.9	0.99	2.14×10^{-4}	31.709	0.97	29851.79	0.0297	0.99	65.6	5.01×10^{5}	1.2	0.99	0.52	4.62	0.075	0.99